SCIENCE CHINA
Technological Sciences

•Article•

March 2022 Vol.65 No.3: 553–568
https://doi.org/10.1007/s11431-021-1944-y

Synergistic control of soft robotic hands for human-like grasp postures

ZHANG NingBin[1], ZHAO Yi[1], GU GuoYing[1,2*] & ZHU XiangYang[1,2]

[1] *Robotics Institute, School of Mechanical Engineering, Shanghai Jiao Tong University, Shanghai 200240, China;*
[2] *State Key Laboratory of Mechanical System and Vibration, Shanghai Jiao Tong University, Shanghai 200240, China*

Received August 19, 2021; accepted October 12, 2021; published online January 27, 2022

Although significant advances in the design of soft robotic hands have been made to mimic the structure of the human hands, there are great challenges to control them for coordinated and human-like postures. Based on the principle of postural synergies in the human hand, we present a synergistic approach for coordinated control of a soft robotic hand to replicate the human-like grasp postures. To this end, we firstly develop a kinematic model to describe the control variables and the various postures of the soft robotic hand. Based on the postural synergies, we use the developed model and Principal Component Analysis (PCA) method to describe the various postures of the soft robotic hand in a low-dimensional space formed by the synergies of actuator motions. Therefore, the coordinates of these synergies can be used as low-dimensional control inputs for the soft robotic hand with a higher-dimensional postural space. Finally, we establish an experimental platform on a customized soft robotic hand with 6 pneumatical actuators to verify the effectiveness of the development. Experimental results demonstrate that with only a 2-dimensional control input, the soft robotic hand can reliably replicate 30 grasp postures in the Feix taxonomy of the human hand.

soft robotic hand, synergistic control, human-like grasp postures, principal component analysis, pneumatic actuation

Citation: Zhang N B, Zhao Y, Gu G Y, et al. Synergistic control of soft robotic hands for human-like grasp postures. Sci China Tech Sci, 2022, 65: 553–568, https://doi.org/10.1007/s11431-021-1944-y

1 Introduction

Human hands have many degrees of freedom (DoFs), which offers much dexterity to perform skilful grasps. When a human hand grasps objects, all finger joints are closely coordinated, which poses a challenge for the design of a robotic hand to replicate human-like grasp postures [1]. A traditional approach to address this challenge is to implement polyarticular structures and multiple actuators in robotic hands [2–5]. However, such designs are generally complex and require sophisticated control strategies, which limit their applications.

In general, during grasping, a human hand usually conforms to the shape of objects without very sophisticated control. The characteristic is partly attributed to the underactuated mechanisms in the hand anatomy, which has inspired effectual underactuated designs for robotic hands [6,7]. However, these designs are usually complicated because the components are primarily rigid and discretely deployed. Recently, soft robotics technology has provided a promising alternative for the underactuated design of robotic hands. Different from rigid components (e.g., joints and links) with compliant structures, soft robotic hands are inherent underactuated due to the compliant feature of the used soft materials. This feature makes the grasping actuation of soft robotic hands result from simple deformations of the structure (e.g., fibre-reinforced chambers [8–10], flexible bellows [11–14] and pouches [15]), which essentially differs from that of the rigid robotic hands. Significant work includes anthropomorphic hands (e.g., RBO Hand II [8], Op-

*Corresponding author (email: guguoying@sjtu.edu.cn)

toelectronically Innervated Soft Hand [9] and BCL-26 Hand [10]) and grippers (e.g., Biological Sampling Gripper [16] and Jamming-based Gripper [17]).

Although significant advances have been made in building soft robotic hands that mimic the structure of the human hand, efforts to control these hands to achieve coordinated, human-like postures are limited. In most anthropomorphic soft hands, multiple actuators are independently controlled [8–10]. As a result, many control signals need to generate to coordinate these actuators for desired postures, which is not available in many cases with limited channels (e.g., user-driven robotic grasping [18]). It has been a great challenge to design an effective coordinated control strategy that can allow the soft robotic hand to replicate a wide range of human-like postures while minimizing control inputs.

A potential approach to develop coordinated control strategies is to imitate the control of the human hands. Neuroscience studies indicate that the human hands' versatile postures are generally controlled within a low-dimensional space, termed as postural synergies [19]. Inspired from this concept, a large amount of interesting work on synergistic control of rigid robotic hands has been reported [4,20–26], which can be broadly divided into two categories. The first category is to design algorithms extracting motion synergies from the data of the human hand or the robotic hand to control a multi-DoF robotic hand without changing its mechanical structures (e.g., the number of actuators). Significant examples of algorithm-based implementation include the synergistic control of the 20-DoF DEXMART Hand [4] and the 12-DoF DLR Hand II [20]. The algorithm-based implementation can also be integrated with dexterous prosthetic hands [21] for amputees with limited control channels. The second category is to mechanically implement synergies into robotic hands to reduce the number of controlled actuators and the hardware complexity, as pioneered by Brown and Asada [23], Xu et al. [24], Xiong et al. [25]. Whether it is an algorithmic or mechanical based implementation, synergistic control has shown great potential in generating more human-like motions for rigid robotic hands with a low number of control inputs.

However, developing synergistic control approaches for soft robotic hands remians elusive. First, the actuation mechanisms and mechanical structures of soft robotic hands differ from those of their rigid analogues, resulting in the difference of kinematic modelling for synergistic control. As shown in Figure 1, rigid robotic hands typically have transmission mechanisms (e.g., tendons, linkages, and gears) to transmit the motion/force of motors into the linkage-based joints. Soft robotic hands usually have soft actuators embedded in the hand structure to transmit the power of stimuli (air pressures in most cases) into the motion/force of actuators themselves, which can be regarded as an integration of transmission mechanisms and end-effectors. Second, soft actuators typically have nonlinear motion-stimuli relationships, which introduces extra calibration and calculation complexity to relate the hand joint angles to the stimuli of actuators [8]. Third, due to the absent synergies that belong to the higher-dimensional space, rigid robotic hands controlled by low-dimensional synergies may have excessive joint angle errors for some postures [4]. It is unclear whether

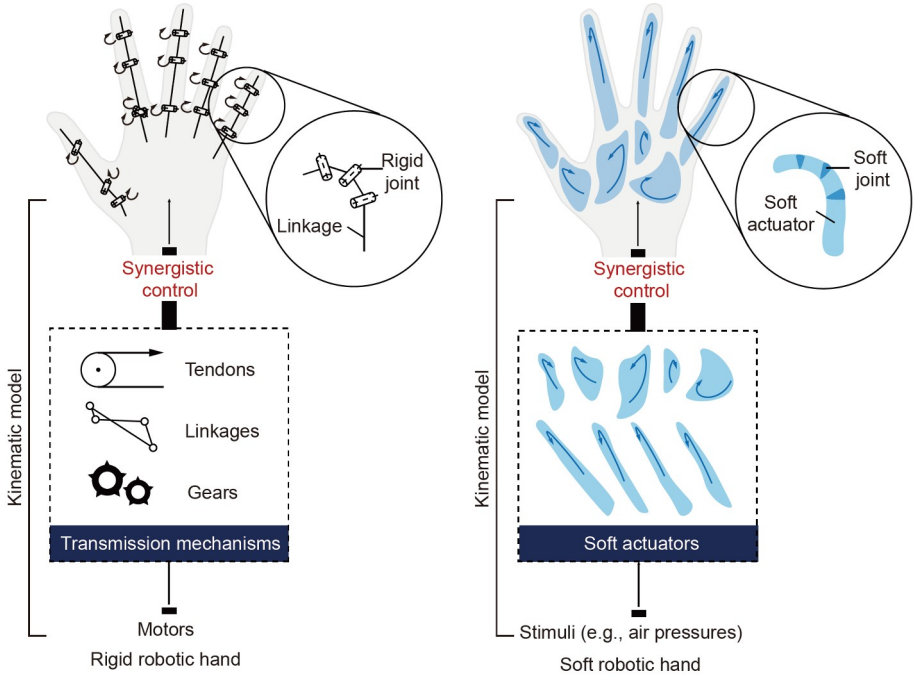

Figure 1 (Color online) Comparison of rigid robotic hands and soft robotic hands on actuation mechanisms and mechanical structures.

the inherent compliance of a soft robotic hand helps compensate for these errors. At last, although there are several "soft" robotic hands designed and controlled with the approach of "soft synergies" or the "adaptive synergies" [26], these approaches are developed based on robotic hands composed of rigid phalanges and tendon-driven mechanisms but with compliant joints or skins (e.g., the Pisa/IIT hands [26]). This is different from the "soft robotic hands" (mainly built with soft materials) in this paper.

To address these challenges, we develop a synergistic control approach derived from postural synergies in the human hand, enabling dexterous soft robotic hands to replicate various human-like grasp postures. We first develop a kinematic model based on the actuation mechanisms and mechanical structures of a soft robotic hand with 6 actuators to describe the relationship between its motion outputs (i.e., postures) and actuation inputs (i.e., pressures). To obtain the required postures, we use a joint-to-joint mapping to transfer measured posture data of the human hand to a high-dimensional posture space of the soft robotic hand. We further leverage a PCA method to approximatively describe the high-dimensional posture space with a low-dimensional synergy space. In this sense, low-dimensional coordinates of the synergy space are used to control the soft robotic hand to achieve high-dimensional grasp postures. Finally, an experimental platform is established for the nonlinear characterization of motion-stimuli relationships of actuators and the effectiveness validation of the developed synergistic control approach. Experimental results demonstrate that with a 2-dimensional control input (i.e., synergy coordinates), the soft robotic hand can replicate 30 postures in the Feix taxonomy of the human hand grasps and the hand's inherent compliance helps compensate for the errors caused by absent synergies.

The remainder of this paper is organized as follows. Sect. 2 presents the modelling of the synergistic control approach, including a brief introduction of a pneumatic, soft robotic hand, its kinematics, and a dimensionality reduction method based on synergies to simplify the robotic hand's task space. Sect. 3 illustrates the generation of synergy coordinates based on measured data of human hand postures. Sect. 4 demonstrates the experimental characterization and validations of the synergistic control approach, and the conclusions are drawn in Sect. 5.

2 Modelling of the synergistic control approach

Our goal is to control the soft robotic hand to replicate human-like grasp postures synergistically. In this section, we first give a brief introduction of a soft robotic hand with 6 pneumatic actuators and underactuated mechanisms. As shown in Figure 2, we build a kinematic model of the soft robotic hand to describe the relationships of its postures (i.e., the joint angle space) and actuation signals. Because the required postures of the soft robotic hand (i.e., the high-dimensional, desired task space) are derived from the data of human hand postures, we use a joint-to-joint mapping scheme between the two hands. We further employ a PCA method to extract synergies of the desired task space to generate a low-dimensional, designed task space. As a result, the corresponding synergy coordinates are used as control inputs for the soft robotic hand to achieve high-dimensional grasp postures.

2.1 Description of the soft robotic hand

The soft robotic hand is developed in our prior work [27]

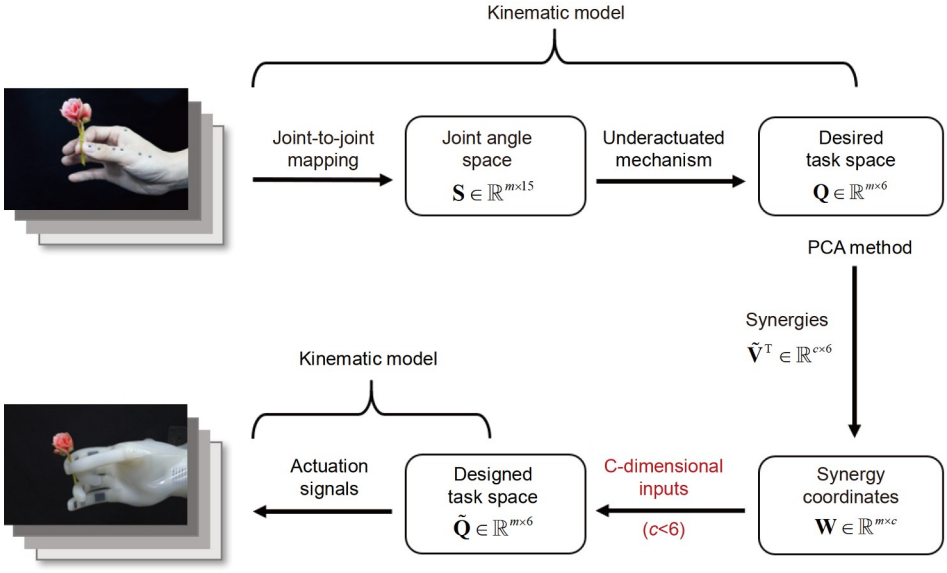

Figure 2 (Color online) Block diagram of the synergistic control approach.

with an anthropomorphic appearance and size (width: 90 mm, length from the wrist: 190 mm), which is beneficial to replicating human-like grasp postures. As shown in Figure 3, the soft robotic hand consists of six soft pneumatic actuators and a rigid palm skeleton. Two types of actuators that bend in different patterns upon pressurization are used to build the hand: one is a multi-joint finger actuator, and the other is a single-joint actuator.

As shown in Figure 3(a), the multi-joint finger actuator has a multi-layered, fibre-reinforced tubular structure integrating soft joints and rigid segments. Upon pressurization, the radial reinforcements (i.e., fibre windings) limit the radial expansion of the elastomeric, hollow inner tube (made of silicone rubber Dragonskin 10, Smooth-On Inc., USA). The strain-limiting layer (i.e., polyethylene mesh) and rigid segments (i.e., carbon fibre plates) inhibit the extension of the tube bottom surface to make the inner tube bend, resembling the articular flexion of human fingers. In this sense, the portions without rigid segments can be regarded as soft joints. An elastomeric outer wrappage (make of silicone rubber Ecoflex 0030, Smooth-On Inc., USA) covers the inner tube to provide cosmetic sealing. The actuator is used as index finger/middle finger/ring finger/little finger (with 3 joints) and thumb (with 2 joints).

As shown in Figure 3(b), the single-joint actuator, termed thumb-palm connection, is a fibre-reinforced elastomeric pad to offer thumb circumduction motion. Upon pressurization, the radial reinforcements (i.e., fibre windings) limit the radial expansion of the elastomeric, hollow pad (made of silicone rubber Dragonskin 10). An elastomeric outer wrappage (made of silicone rubber Ecoflex 00-30) covers the inner pad to provide cosmetic sealing. The strain-limiting layer (i.e., polyethylene mesh) inhibits the extension of the pad's bottom surface to make the pad bend, imitating the circumduction motion of the human thumb.

As shown in Figure 3(c) and (d), the soft robotic hand has 6 active flexion DoFs and 15 soft joints. We number the carpal-metacarpal (CMC) joint, metacarpal-phalangeal (MCP) joint, and interphalangeal (IP) joint of the opposable thumb as joints 1, 2, and 3, respectively. We number the MCP joint, proximal interphalangeal (PIP) joint, and distal interphalangeal (DIP) joint of the index finger as joints 4, 5, and 6, respectively. The joint numbering of the middle finger/ring finger/little finger is similar to that of the index finger.

Furthermore, the inherent compliance of the soft actuators introduces various passive DoFs to the hand, mimicking the passive compliance of the human hand. For example, the soft robotic hand has no active abduction/adduction DoFs between fingers, but the actuator compliance enables their passive abduction/adduction. In this sense, the control

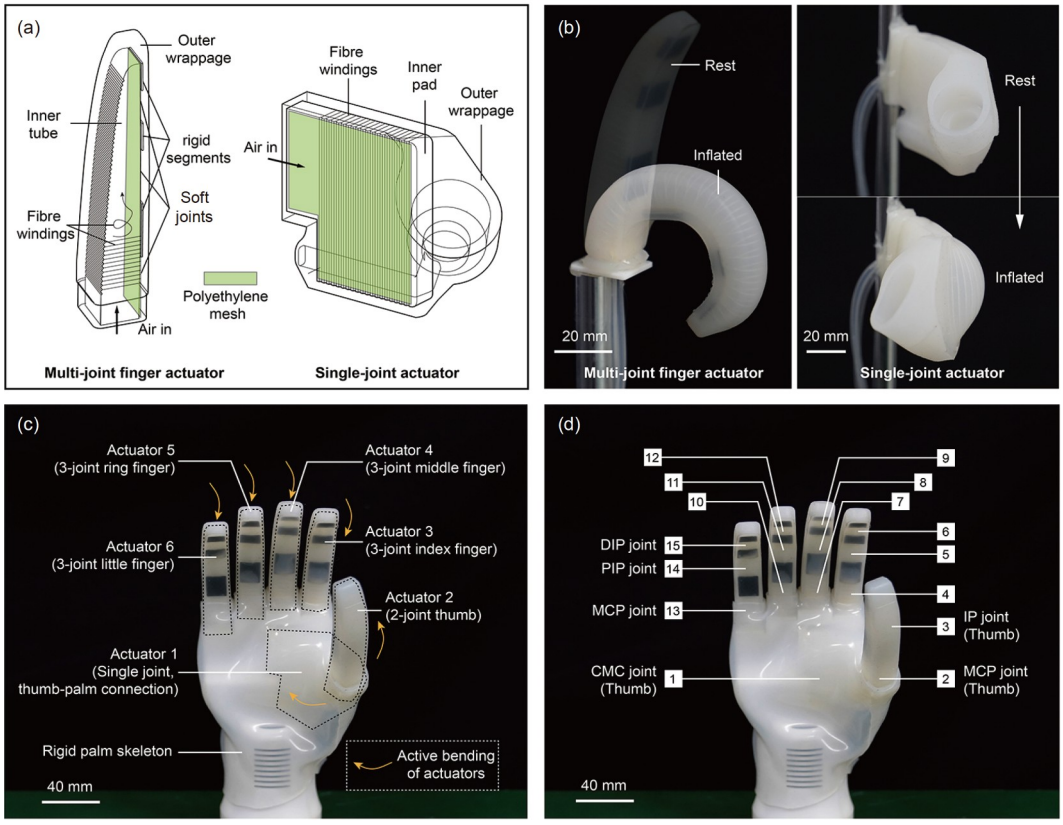

Figure 3 (Color online) Schematic of the soft robotic hand. (a) Structure of the multi-joint finger actuator and the single-joint actuator; (b) the rest state and inflated state of the two kinds of actuators; (c) location of the actuators in the soft robotic hand prototype; (d) location and numbering of the soft joints.

complexity of the soft robotic hand is reduced, which potentially helps dexterous, adaptive grasping.

2.2 Kinematic model

The flexion angle of a joint in the soft robotic hand is denoted as s. Thus, a grasp posture of the soft robotic hand can be described by a vector $\mathbf{s} = (s_1 \ \ s_2 \ \cdots \ s_{15}) \in \mathbb{R}^{15}$, where s_k $(k = 1, 2, \cdots 15)$ denotes the k-th joint angle. The flexion of 15 joints results from the bending of 6 actuators. We define the bending angle of an actuator as q. Thus, $\mathbf{s}$ can be deduced by a vector $\mathbf{q} = (q_1 \ \ q_2 \ \cdots \ q_6) \in \mathbb{R}^6$, where q_i denotes the i-th actuator bending angle.

As shown in Figure 3(c) and (d), only the CMC joint is independently actuated (i.e., driven by the thumb-palm connection) while others are underactuated (i.e., driven by the multi-joint finger actuators). According to the actuator and joint numbers listed in Figure 3(c) and (d), we establish a piecewise mapping between q_i and s_k:

$$\begin{aligned} &q_1 = s_1; \ \ q_2 = s_2 + s_3; \\ &q_i = \sum_{k=3i-5}^{3i-3} s_k \quad (i = 3, 4, 5, 6). \end{aligned} \tag{1}$$

The postures can be written as a matrix form ($\mathbf{S}$, termed joint space):

$$\mathbf{S} = (\mathrm{s}_1 \ \ \mathrm{s}_2 \ \cdots \ \mathrm{s}_m)^{\mathrm{T}} \in \mathbb{R}^{m \times 15}, \tag{2}$$

where m denotes the total number of grasp postures and $\mathbf{s}_j = (s_{j,1} \ \ s_{j,2} \ \cdots \ s_{j,15}) \in \mathbb{R}^{15}$ denotes joint angles of the j-th grasp posture. Likewise, the postures can also be described by m groups of actuator bending angles ($\mathbf{Q}$, termed task space):

$$\mathbf{Q} = (\mathbf{q}_1 \ \ \mathbf{q}_2 \ \cdots \ \mathbf{q}_m)^{\mathrm{T}} \in \mathbb{R}^{m \times 6}, \tag{3}$$

where $\mathbf{q}_j = (q_{j,1} \ \ q_{j,2} \ \cdots \ q_{j,6})$ denotes actuator bending angles of the j-th grasp posture.

Since we aim to using the robotic hand to achieve human-like grasp postures, it is necessary to map the human hand postures onto $\mathbf{Q}$. The data of human hand joint angles can be acquired by a visual capture system as we use in this paper, or other motion capture devices (e.g., Cybergloves [25]). According to Feix et al. [28], the human hand has more than 20 DoFs, which is more than that of the soft robotic hand. To address such a kinematic dissimilarity between the soft robotic hand and the human hand, only the joint angles existing in both hands are tracked (via direct or indirect ways, see Sect. 3). Thus, a joint-to-joint mapping [29] is leveraged to transfer the joint angles of the human hand to those of the soft robotic hand. By combining eqs. (1)–(3), one can yield the desired task space of the soft robotic hand.

Finally, we investigate the relationship between the actuator bending angle and its input pressure. The pressure of the i-th actuator p_i can be written as a function of q_i:

$$p_i = f_i(q_i). \tag{4}$$

The function f_i, governed by the actuator design, is typically nonlinear and obtained by experimental characterization in free space [8,10]. Thus, for each actuator, we can use eq. (4) to calculate the pressures corresponding to different bending angles.

2.3 Dimensionality reduction with synergies

When m increases, the dimensionality of the desired task space $\mathbf{Q}$ becomes quite large, which introduces much control complexity. A promising method for simplification is to represent $\mathbf{Q}$ within a lower-dimensional space, mimicking the postural synergies in the human hand. To this end, we leverage the Principal Component Analysis (PCA) [30] to extract lower-dimensional synergies of $\mathbf{Q}$, and use them for the practical implementation in the soft robotic hand. The process is described as follows. First, the i-th actuator bending angles for m grasp postures described in $\mathbf{Q}$ are averaged:

$$\overline{q}_i = \frac{1}{m} \sum_{j=1}^{m} q_{j,i}. \tag{5}$$

Thus, $\mathbf{Q}$ can be expressed as the sum of two parts:

$$\begin{aligned} \mathbf{Q} &= \mathbf{X} + \overline{\mathbf{Q}} \\ &= \begin{pmatrix} x_{1,1} & x_{1,2} & \cdots & x_{1,6} \\ x_{2,1} & x_{2,2} & \cdots & x_{2,6} \\ \vdots & \vdots & \ddots & \vdots \\ x_{m,1} & x_{m,2} & \cdots & x_{m,6} \end{pmatrix} + \begin{pmatrix} \overline{q}_1 & \overline{q}_2 & \cdots & \overline{q}_6 \\ \overline{q}_1 & \overline{q}_2 & \cdots & \overline{q}_6 \\ \vdots & \vdots & \ddots & \vdots \\ \overline{q}_1 & \overline{q}_2 & \cdots & \overline{q}_6 \end{pmatrix}, \end{aligned} \tag{6}$$

where $\mathbf{X} \in \mathbb{R}^{m \times 6}$ denotes the dataset of actuator bending angle deviations and $\overline{\mathbf{Q}} \in \mathbb{R}^{m \times 6}$ indicates the dataset of averaged actuator bending angles across m postures. Each row of $\overline{\mathbf{Q}}$ (i.e., $(\overline{q}_1 \ \ \overline{q}_2 \ \cdots \ \overline{q}_6)$) represents the average posture of the soft robotic hand across m postures. According to the Singular Value Decomposition (SVD) [31], $\mathbf{X}$ can be expressed as the product of three parts:

$$\mathbf{X} = \mathbf{U}\mathbf{A}\mathbf{V}^{\mathrm{T}}, \tag{7}$$

where $\mathbf{U} \in \mathbb{R}^{m \times m}$ and $\mathbf{V}^{\mathrm{T}} \in \mathbb{R}^{6 \times 6}$ are unitary matrixes, and $\mathbf{A} \in \mathbb{R}^{m \times 6}$ is a positive semidefinite rectangular diagonal matrix. Each element on the diagonal of $\mathbf{A}$ is denoted as a singular value λ_c $(c = 1, 2, \cdots, 6)$. Each column of $\mathbf{V}$ is the principal component [30] of $\mathbf{X}$ and can be expressed as $\mathbf{V} = (\mathbf{v}_1 \ \ \mathbf{v}_2 \ \cdots \ \mathbf{v}_6)$. The proportional relationship of six elements in vector $\mathbf{v}_c$ denotes the coordinated characteristics of actuator flexion angle deviations, which can be regarded as a synergy. Then, the variance of $\mathbf{X}$, namely λ_c^2, is used to calculate the contribution rate of the c-th synergy:

$$\eta_c = \lambda_c^2 / \sum_{C=1}^{6} \lambda_C^2. \tag{8}$$

Furthermore, the cumulative contribution rate of the first c synergies is calculated as

$$\hat{\eta}_c = \sum_{C=c}^{c} \lambda_C^2 / \sum_{C=1}^{6} \lambda_C^2. \tag{9}$$

Because λ_c^2 is listed in descending order by the contribution rate in SVD [31], we use the first c synergies to generate a matrix $\widetilde{\mathbf{X}} \in \mathbb{R}^{m\times 6}$ to describe $\mathbf{X}$ approximatively:

$$\mathbf{X} \approx \widetilde{\mathbf{X}} = \widetilde{\mathbf{U}}\widetilde{\mathbf{A}}\widetilde{\mathbf{V}}^{\mathrm{T}}, \tag{10}$$

where $\widetilde{\mathbf{U}} \in \mathbb{R}^{m\times c}$, $\widetilde{\mathbf{A}} = \mathrm{diag}(\lambda_1 \ \lambda_2 \ \cdots \ \lambda_c) \in \mathbb{R}^{c\times c}$, and $\widetilde{\mathbf{V}}^{\mathrm{T}} = (\mathbf{v}_1 \ \mathbf{v}_2 \ \cdots \ \mathbf{v}_c)^{\mathrm{T}} \in \mathbb{R}^{c\times 6}$, respectively. We further define a matrix $\mathbf{W} \in \mathbb{R}^{m\times c}$ as

$$\mathbf{W} = \widetilde{\mathbf{Y}}\widetilde{\mathbf{A}}. \tag{11}$$

Substituting eqs. (10) and (11) into eq. (6) yields a designed task space $\widetilde{\mathbf{Q}} \in \mathbb{R}^{m\times 6}$:

$$\begin{aligned}\widetilde{\mathbf{Q}} &= \mathbf{W}\widetilde{\mathbf{V}}^{\mathrm{T}} + \overline{\mathbf{Q}} \\ &= (\mathbf{w}_1 \ \mathbf{w}_2 \ \cdots \ \mathbf{w}_c)(\mathbf{v}_1 \ \mathbf{v}_2 \ \cdots \ \mathbf{v}_c)^{\mathrm{T}} \\ &\quad + (\overline{\mathbf{q}}_1 \ \overline{\mathbf{q}}_2 \ \cdots \ \overline{\mathbf{q}}_6).\end{aligned} \tag{12}$$

The elements in the vector $\mathbf{w}_\xi$ ($\xi = 1, 2, \cdots, c$) are the coefficients of synergy $\mathbf{v}_\xi$ for different postures. Eq. (12) indicates that the c-dimensional space formed by c synergies can describe $\widetilde{\mathbf{Q}}$. In other words, the c-dimensional coefficients can be regarded as inputs to control the soft robotic hand to achieve human-like postures. Therefore, the coefficients are termed synergy coordinates. In this way, the dimensionality of control inputs can be reduced from 6 to c. Additionally, eq. (12) can be expanded as

$$\begin{pmatrix} \tilde{q}_{1,1} & \tilde{q}_{1,2} & \cdots & \tilde{q}_{1,6} \\ \tilde{q}_{2,1} & \tilde{q}_{2,2} & \cdots & \tilde{q}_{2,6} \\ \vdots & \vdots & \ddots & \vdots \\ \tilde{q}_{m,1} & \tilde{q}_{m,2} & \cdots & \tilde{q}_{m,6} \end{pmatrix} = \begin{pmatrix} w_{1,1} & w_{1,2} & \cdots & w_{1,c} \\ w_{2,1} & w_{2,2} & \cdots & w_{2,c} \\ \vdots & \vdots & \ddots & \vdots \\ w_{m,1} & w_{m,2} & \cdots & w_{m,c} \end{pmatrix}$$
$$\times \begin{pmatrix} v_{1,1} & v_{1,2} & \cdots & v_{1,c} \\ v_{2,1} & v_{2,2} & \cdots & v_{2,c} \\ \vdots & \vdots & \ddots & \vdots \\ v_{6,1} & v_{6,2} & \cdots & v_{6,c} \end{pmatrix}^{\mathrm{T}} + \begin{pmatrix} \overline{q}_1 & \overline{q}_2 & \cdots & \overline{q}_6 \\ \overline{q}_1 & \overline{q}_2 & \cdots & \overline{q}_6 \\ \vdots & \vdots & \ddots & \vdots \\ \overline{q}_1 & \overline{q}_2 & \cdots & \overline{q}_6 \end{pmatrix}. \tag{13}$$

According to eq. (13), the flexion angle of the i-th actuator for the j-th posture is obtained:

$$\begin{aligned}\tilde{q}_{j,i} &= \begin{pmatrix} w_{j,1} & w_{j,2} & \cdots & w_{j,c} \end{pmatrix} \\ &\quad \times \begin{pmatrix} v_{1,i} & v_{2,i} & \cdots & v_{c,i} \end{pmatrix}^{\mathrm{T}} + \overline{q}_i.\end{aligned} \tag{14}$$

Substituting eqs. (4) and (14) into $\widetilde{\mathbf{Q}}$ yields the actuation space $\widetilde{\mathbf{P}} \in \mathbb{R}^{m\times 6}$:

$$\widetilde{\mathbf{P}} = \begin{pmatrix} f_1(\tilde{q}_{1,1}) & f_2(\tilde{q}_{1,2}) & \cdots & f_6(\tilde{q}_{1,6}) \\ f_1(\tilde{q}_{2,1}) & f_2(\tilde{q}_{2,2}) & \cdots & f_6(\tilde{q}_{2,6}) \\ \vdots & \vdots & \ddots & \vdots \\ f_1(\tilde{q}_{m,1}) & f_2(\tilde{q}_{m,2}) & \cdots & f_6(\tilde{q}_{m,6}) \end{pmatrix}. \tag{15}$$

The elements of $\widetilde{\mathbf{P}}$ are the actuation signals for designed postures of the soft robotic hand. Thus, we can use c-dimensional synergy coordinates to control the soft robotic hand to replicate multiple human-like postures, which is termed the synergistic control approach. In the following Sects. 3 and 4, we present an example in which m=33 (all 33 typical grasp postures in the Feix taxonomy [28]) to demonstrate the effectiveness of the approach with the anthropomorphic hand introduced in Sect. 2.

3 Generating synergy coordinates based on human hand postures

In this section, we first use a motion capture system to acquire the posture data of the human hand, followed by the calculation of human hand joint angles. Afterwards, we use the approach illustrated in Sect. 2 to calculate the synergy coordinates.

3.1 Calculation of the desired task space

We perform experiments on the grasping behaviour of the human hand to create a reference posture dataset for $\widetilde{\mathbf{Q}}$. Here, we choose the postures in the Feix taxonomy [28] as the grasping paradigms. The Feix taxonomy is chosen because it covers the most extensive set of static, stable human grasp postures (m = 33) among the previous work.

Six healthy subjects (four males and two females) volunteers for the grasp experiments. Their hand sizes (average width: 86 mm, average length from the wrist: 183 mm) are similar to the soft robotic hand. The subjects are provided informed consent prior to participating in the experiment. The experiment procedure is in accordance with the Declaration of Helsinki. Before the experiments, a subject is instructed to train for about 30 min, in which the subject tries particular postures to grasp customized objects following the Feix taxonomy (see Figure 4(a)).

During the experiments, the posture dataset of the human hand is acquired using a Prime 13 motion capture system (OptiTrack Inc., USA). As shown in Figure 4(b), a total of 29 reflective markers are attached to the hand of a volunteer, including 6 markers on the thumb, 4 markers on the index/middle/ring/little finger, 6 markers on the back of the hand and 1 marker located between the thumb and the index finger. A total of 6 cameras are deployed around the volunteer so that at least two of them capture the motion of all markers at a single time instance. The motion capture system has a resolution of 1.3 MP (1280 × 1024) and a frame rate of 240 FPS. The subject sits naturally, grasping a customized object delivered by an assistant with the corresponding grasp posture defined by the Feix taxonomy. Each grasp posture is held for 10 s and the cameras record the positions of the

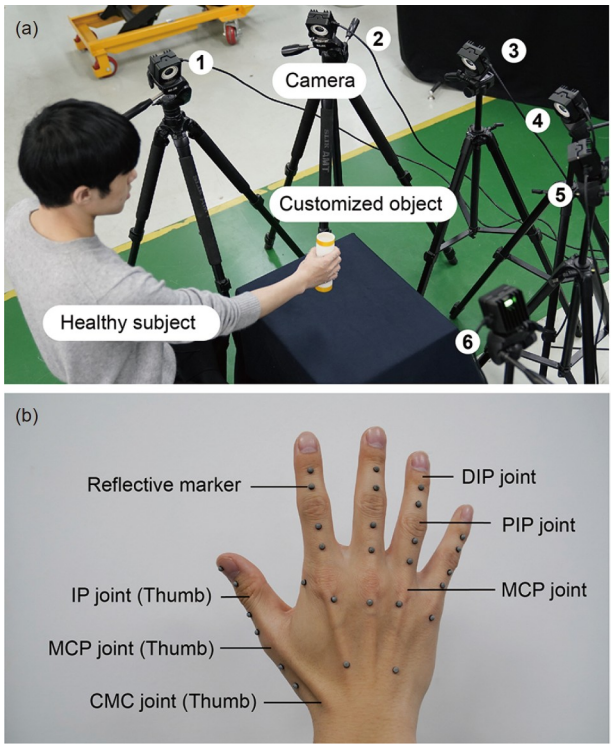

Figure 4 (Color online) A visual tracking method is used to acquire human hand postures. (a) Experimental setup; (b) the distribution of reflective markers.

markers. All 33 grasp postures are measured (see Figure 5). Each posture is sampled 3 times for establishing repeatability and relevance of trends, and the values are averaged to generate a dataset.

Based on the dataset, we calculate the joint angles of the human hand, which can be categorized into three kinds. The first kind of joint angle is generated by two vectors. Such kind of joint angle includes the flexion of PIP joints (index finger, middle finger, ring finger, and little finger), MCP joint (thumb), and IP joint (thumb). As shown in Figure 6(a), the joint angle can be deduced by

$$\theta = \cos^{-1}\left(\frac{\mathbf{u}_1 \cdot \mathbf{u}_2}{|\mathbf{u}_1||\mathbf{u}_2|}\right), \tag{16}$$

where $\mathbf{u}_1=\mathbf{a}_1-\mathbf{a}_2$, $\mathbf{u}_2=\mathbf{a}_3-\mathbf{a}_4$ and $\mathbf{a}_t$ (t=1,2,3,…) denotes the three-dimensional coordinate of each marker. As shown in Figure 6(b), the second kind of joint angle is generated by a vector and a plane (i.e., Plane I). Such kind of joint angle includes the flexion of MCP joints (index finger, middle finger, ring finger, and little finger). The joint angle can be deduced by

$$\theta=\sin^{-1}\left(\frac{\mathbf{u}_1 \cdot \mathbf{n}_1}{|\mathbf{u}_1||\mathbf{n}_1|}\right), \tag{17}$$

where $\mathbf{u}_1=\mathbf{a}_1-\mathbf{a}_2$, $\mathbf{n}_1$ is the normal vector of Plane I ($\mathbf{n}_1=\mathbf{u}_2\times\mathbf{u}_3$, $\mathbf{u}_2=\mathbf{a}_3-\mathbf{a}_4$ and $\mathbf{u}_3=\mathbf{a}_5-\mathbf{a}_6$). As shown in Figure 6(c), the third kind of joint angle (i.e., the circumduction of the thumb's CMC joint) is generated by two planes (i.e., Plane I and Plane II). The joint angle can be deduced by

$$\theta=\cos^{-1}\left(\frac{\mathbf{n}_1 \cdot \mathbf{n}_2}{|\mathbf{n}_1||\mathbf{n}_2|}\right), \tag{18}$$

where $\mathbf{n}_1$ and $\mathbf{n}_2$ are the normal vectors of Plane I and II, respectively ($\mathbf{n}_1=\mathbf{u}_1\times\mathbf{u}_2$, $\mathbf{n}_2=\mathbf{u}_3\times\mathbf{u}_4$, $\mathbf{u}_1=\mathbf{a}_1-\mathbf{a}_2$, $\mathbf{u}_2=\mathbf{a}_3-\mathbf{a}_4$, $\mathbf{u}_3=\mathbf{a}_5-\mathbf{a}_6$ and $\mathbf{u}_4=\mathbf{a}_7-\mathbf{a}_8$).

The flexion of DIP joints (index finger, middle finger, ring finger, and little finger) are not directly calculated because the markers on the fingertips are often obscured during grasping tasks. In this sense, we consider the motion feature of the human hand that the DIP-PIP joint angle relationship is approximately linear for a considerable proportion of grasp postures [32]. According to Fujiki et al. [33] and Magenes et al. [34], we assume the flexion angle of the DIP joint is 2/3 times that of the corresponding PIP joint. Notably, occlusion difficulties can be addressed by Cyberglove-based motion capturing methods and thus flexion of DIP joints can be directly calculated, which will be investigated in our future work. As discussed in Sect. 2.1, the abduction angles

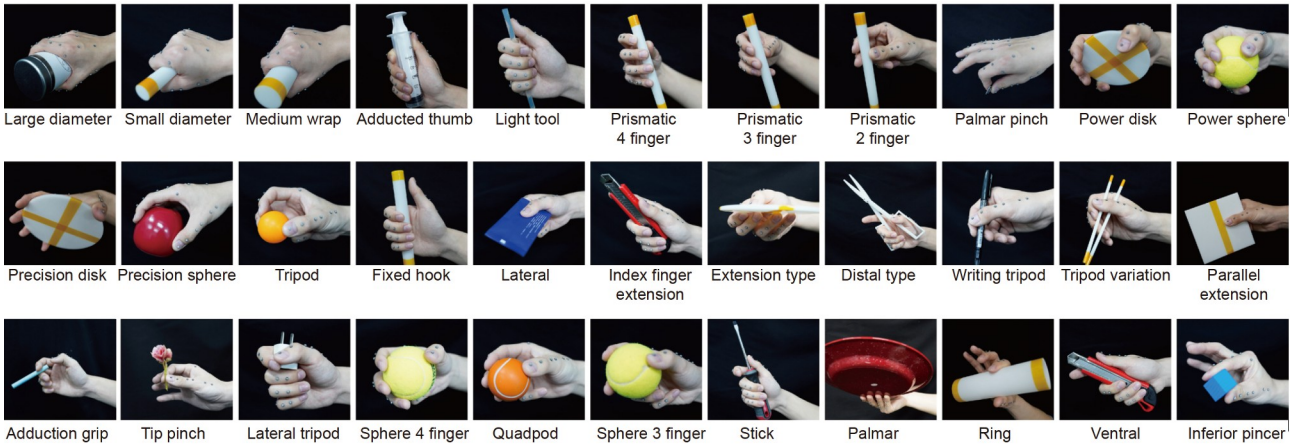

Figure 5 (Color online) Still images of the 33 grasp postures of the human hand.

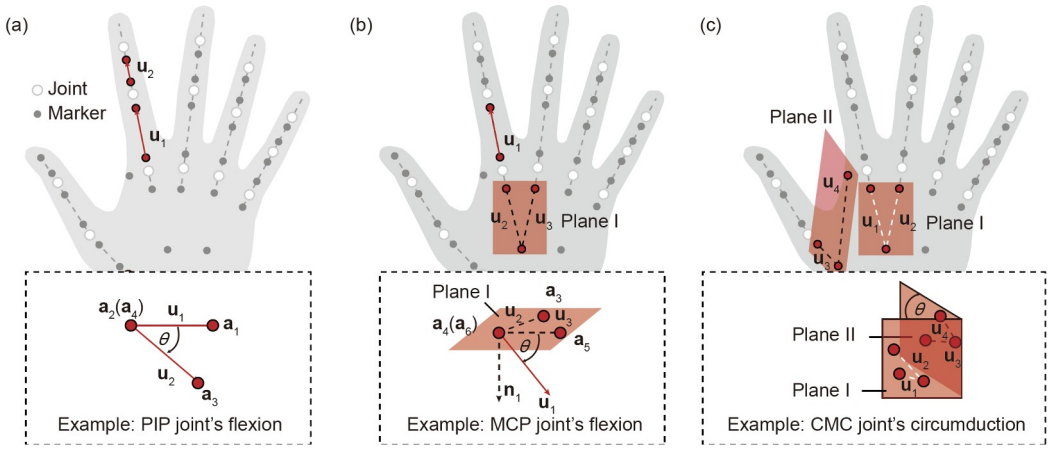

Figure 6 (Color online) Schematics of the three kinds of joint angles. (a) The angle between two vectors; (b) the angle between a vector and a plane; (c) the angle between two planes.

between fingers are not calculated because the soft robotic hand has no corresponding active DoFs. Combining the above calculation results and eqs. (1)–(3), we can obtain the desired task space of the soft robotic hand $\mathbf{Q} \in \mathbb{R}^{33\times 6}$.

3.2 Calculation of the synergy coordinates

According to eq. (5), we obtain the average posture: $\overline{q}_1 = 56.7°$, $\overline{q}_2 = 45.1°$, $\overline{q}_3 = 131.0°$, $\overline{q}_4 = 155.2°$, $\overline{q}_5 = 164.4°$ and $\overline{q}_6 = 171.7°$. Table 1 lists the vectors of 6 synergies obtained by adopting eqs. (6) and (7). The contribution rates of 6 synergies are 80.1%, 9.8%, 6.0%, 2.3%, 1.0%, and 0.8%, respectively. The cumulative contribution rates of 6 synergies are 80.1%, 89.9%, 95.9%, 98.2%, 99.2%, and 100%, respectively. The above results are plotted in Figure 7. The first 2 synergies (i.e., the highlighted vectors in Figure 7(a)) count for 89.9% cumulative contribution rate while others

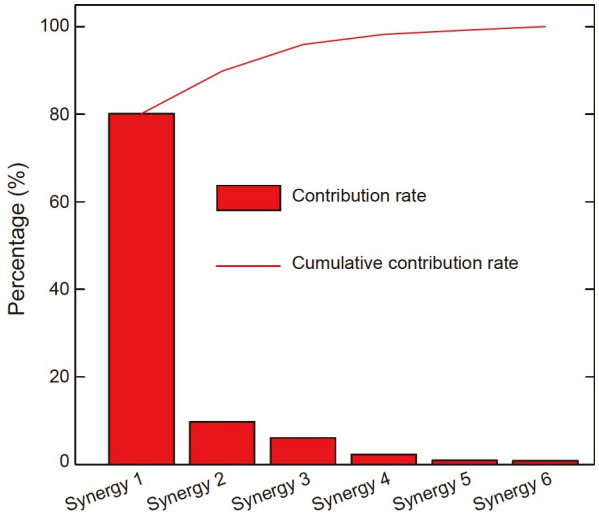

Figure 7 (Color online) The contribution rate and cumulative contribution rate of 6 synergies.

Table 1 The vectors of 6 synergies

Synergy number	Synergy direction
Synergy 1	$[7.8\times10^{-5}\ \ 0.08\ \ 0.28\ \ 0.45\ \ 0.57\ \ 0.62]^{\mathrm{T}}$
Synergy 2	$[0.08\ \ 0.38\ \ 0.85\ \ 0.06\ \ -0.17\ \ -0.32]^{\mathrm{T}}$
Synergy 3	$[0.20\ \ 0.88\ \ -0.33\ \ -0.18\ \ -0.05\ \ 0.21]^{\mathrm{T}}$
Synergy 4	$[-0.32\ \ 0.23\ \ -0.29\ \ 0.65\ \ 0.19\ \ -0.54]^{\mathrm{T}}$
Synergy 5	$[0.90\ \ -0.13\ \ -0.09\ \ 0.15\ \ 0.24\ \ -0.28]^{\mathrm{T}}$
Synergy 6	$[-0.19\ \ 0.07\ \ 0.06\ \ -0.56\ \ 0.74\ \ 0]^{\mathrm{T}}$

only count for 10.1%. Hence, we choose $c = 2$ and use the first 2 synergies to generate the designed task space $\widetilde{\mathbf{Q}} \in \mathbb{R}^{33\times 6}$.

The matrix $\mathbf{W} \in \mathbb{R}^{33\times 2}$ can be calculated by adopting eqs. (10) and (11). The two columns of the matrix $\mathbf{W}$ (i.e., $\mathbf{w}_1$ and $\mathbf{w}_2$) denote the 2-dimensional synergy coordinates corresponding to 33 grasp postures in the designed task space. Note that the synergy coordinates of the average posture are (0, 0). As shown in Figure 8, we plot the synergy coordinates of the 33 grasp postures (marked circle) and the average posture (marked star) in the designed task space formed by the first 2 synergies. The 33 grasp postures in the designed task space do not cluster into several discrete groups, which is essentially consistent with the results in ref. [19].

According to eqs. (12) and (13), we can obtain the actuator bending angles in the designed task space $\widetilde{\mathbf{Q}}$ (formed by the first 2 synergies) and compare them with those in the desired task space $\mathbf{Q}$ (formed by all 6 synergies) as shown in Figure 9. The variation trends of bending angles in both task spaces are the same for almost all actuators except that for the thumb, which indicates that the absence of 4 synergies mostly contributes to the variations of thumb bending angles. We also find that the values are almost positive (i.e., bend-

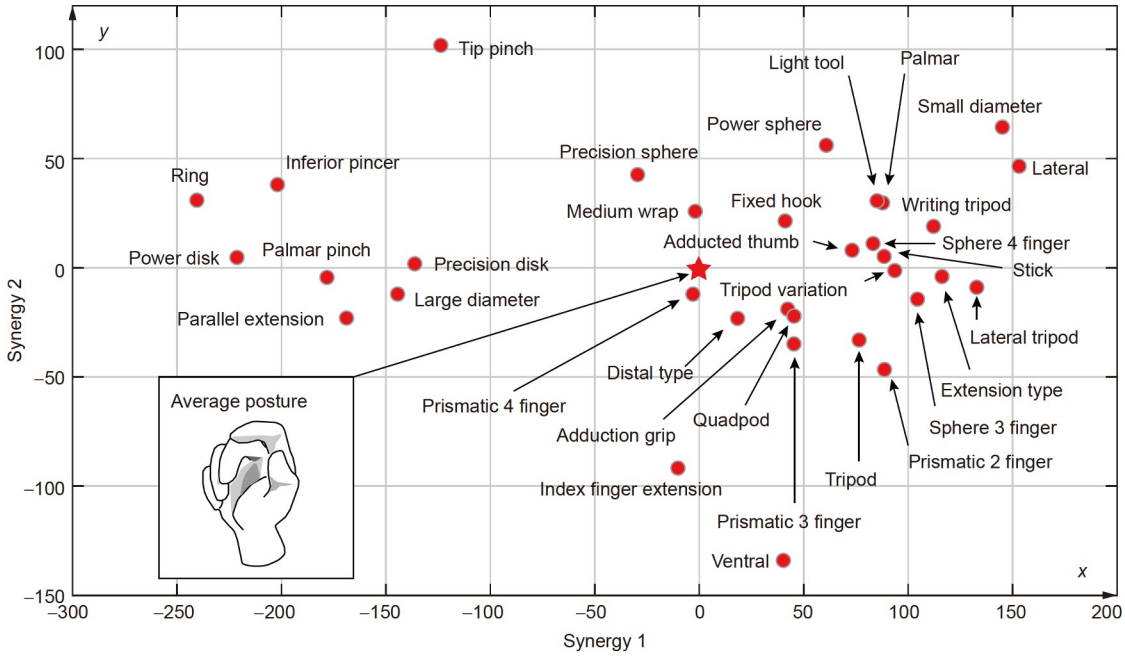

Figure 8 (Color online) The distribution of 33 grasp postures and the average posture in the 2-dimensional space formed by the first 2 synergies.

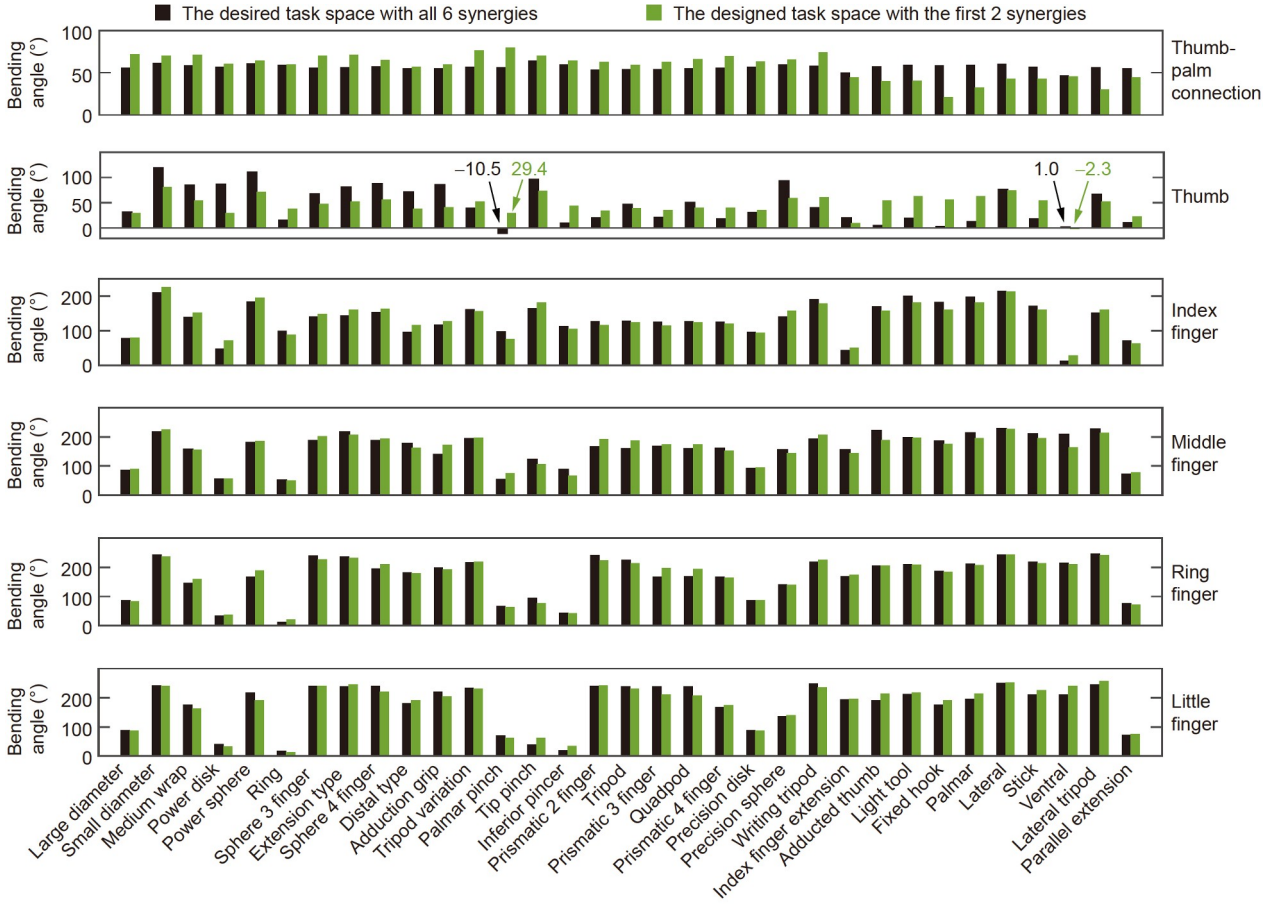

Figure 9 (Color online) Comparison of desired task space (with all 6 synergies) and designed task space (with the first 2 synergies) on actuator bending angles.

ing) except for two special cases of Palmar pinch and Ventral. For Palmar pinch, the value of the thumb bending angle is negative in $\mathbf{Q}$ (i.e., extension as shown in Figure 5) but the corresponding value is positive in $\widetilde{\mathbf{Q}}$ (–10.5° vs. 29.4°). For

Ventral, the value of thumb bending angle is positive in $\mathbf{Q}$ but the corresponding value is negative in $\widetilde{\mathbf{Q}}$ (1.0° vs. –2.3°). Since the negative value in $\widetilde{\mathbf{Q}}$ can not achieve via active control and the value is relatively small, we replace –2.3° with 0° considering the practical fact.

To further quantize the difference between the two task spaces, we calculate their relative errors by

$$e_{j,i} = \frac{\tilde{q}_{j,i} - q_{j,i}}{q_{j,i}}, \tag{19}$$

where the subscript i and j denote the i-th actuator and the j-th posture, respectively. The mean relative error for the i-th actuator is calculated by

$$e_i = \frac{\sum_{j=1}^{33} e_{j,i}}{33}. \tag{20}$$

The results are plotted in Figure 10. The minimum and maximum relative errors occur in the subgraph of thumb, reaching −380.2% and +1922.2%, respectively. The values of mean relative errors are all positive (i.e., +7.2%, +116.4%, +4.1%, +1.1%, +1.8%, and +2.7%), indicating that bending angles in $\widetilde{\mathbf{Q}}$ are larger than those in $\mathbf{Q}$ on average. The mean relative error of thumb is particularly large (>100%) compared with those of other actuators (<10%), which can be attributed to the absence of 4 synergies. Furthermore, we respectively use 2, 3, 4 and 5 synergies to generate designed task spaces and compare the relative error distributions for the thumb. We calculate the minimum (denoted as $e_{j,2,\min}$), maximum (denoted as $e_{j,2,\max}$), mean (i.e., e_2), and range (denoted as $\sigma = e_{j,2,\max} - e_{j,2,\min}$) of relative errors. As shown in Figure 11, with increasing number of synergies, the trends of $e_{j,2,\max}$, e_2 and σ are similar, decreasing from 1922.2% to 14.9%, 116.4% to −2.6%, and 2302.4% to 91.3%, respectively, while $e_{j,2,\min}$ has no obvious trends. Overall, the results indicate that it is helpful to decrease the relative error of thumb bending angles by adding more synergies.

4 Leveraging synergy coordinates to control the soft robotic hand

In this section, we use the synergy coordinates generated in Sect. 3 to drive the soft robotic hand to achieve 33 postures. We first build a pneumatic control platform for the soft robotic hand. Then, we experimentally characterize the bending angle-pressure relationship of the actuators. Based on the synergy coordinates and the results of actuator characterization, we calculate the required pressures to drive the soft

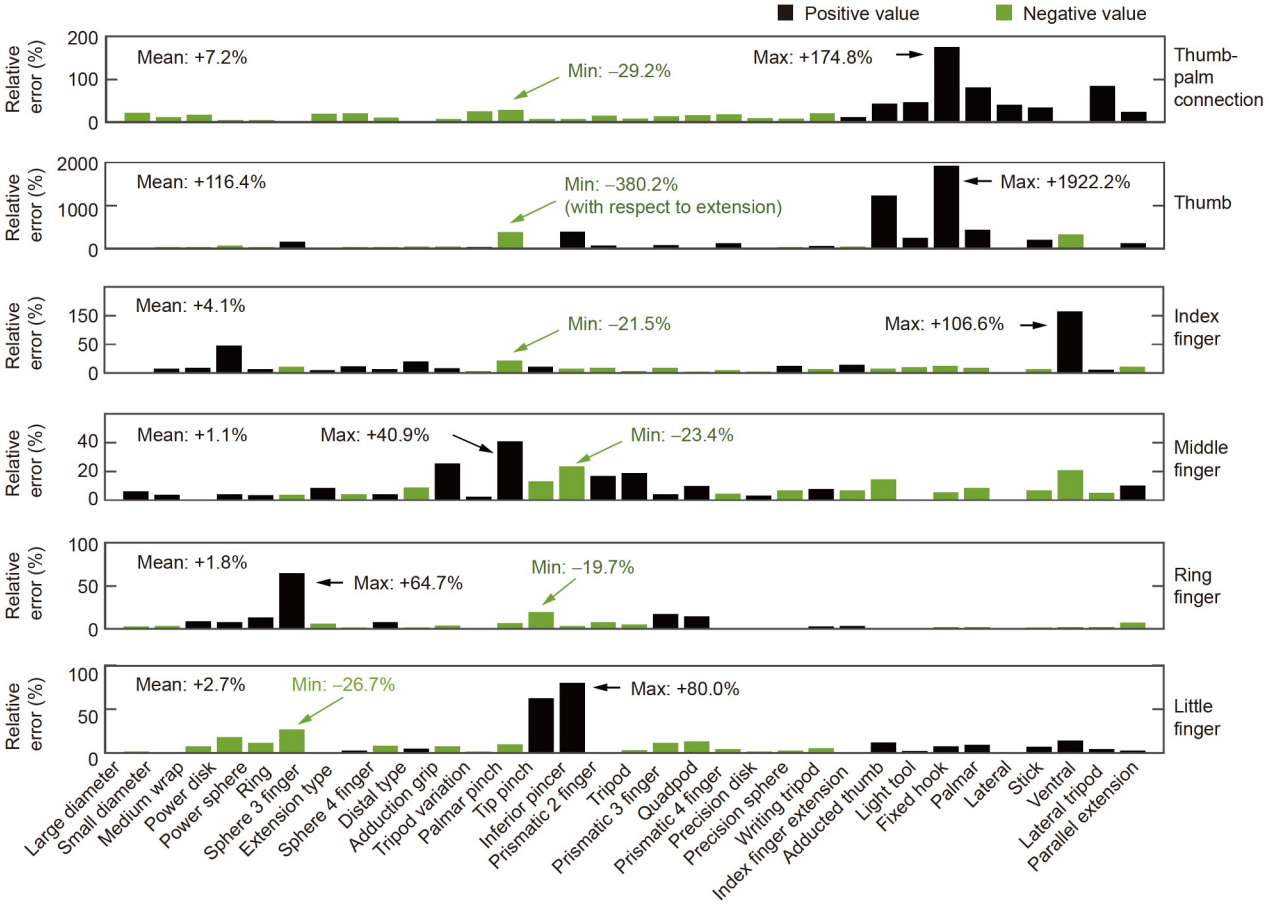

Figure 10 (Color online) Relative errors of bending angles for different actuators of the two task spaces.

robotic hand. Finally, we evaluate the experimental results to demonstrate the effectiveness of the synergistic control approach.

4.1 Control platform

As shown in Figure 12(a), the control platform includes a user interface, a dSPACE-DS1103 board, 6 pressure regulation modules, an air source, and the soft robotic hand. The user interface is created in Matlab (Version 2018b, USA) for users to specify 2-dimensional synergy coordinates. Based on the synergy coordinates, the interface calculates the 6-dimensional pneumatic actuation signals (i.e., pressures) and sends them to a dSPACE-DS1103 board via serial port communication. The dSPACE-DS1103 board leverages digital-to-analogue converters (DAC) to convert the pneumatic actuation signals to voltage signals to drive 6 pressure regulation modules. All the 6 pressure regulation modules are connected to an air source (i.e., the pump, Eidolon, China). As shown in Figure 12(b), a single pressure regulation module consists of an electric proportional regulator (MM1MBHEEN, Proportion-Air, USA) and a pressure sensor (528, HUBA, Switzerland). The electric proportional regulator allows for the regulation of outlet pressures proportionally to the voltage signals, which is based on its self-contained pressure sensors and the bang-bang control strategy [35]. The HUBA pressure sensor is used for checking whether the electric proportional regulator works normally and for sending the measured pressures to the dSPACE-DS1103 board via analogue-to-digital converters (ADCs). Thus, the 6 pressure regulation modules can individually control the pressure of 6 soft actuators connected to them.

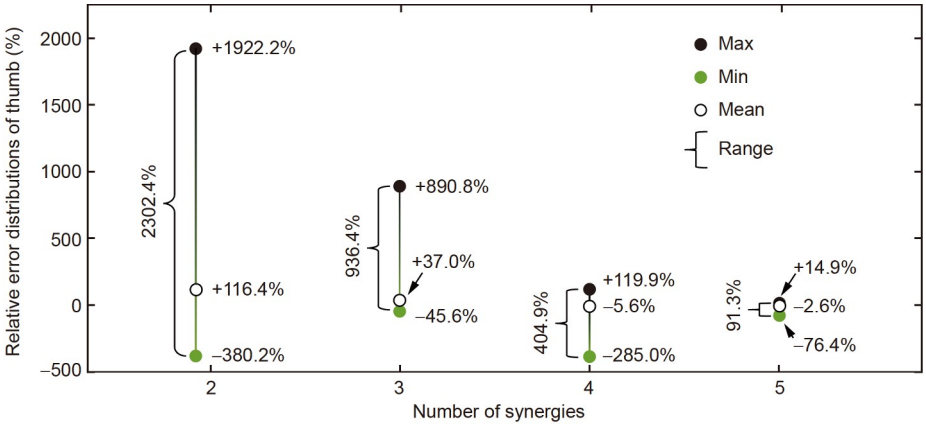

Figure 11 (Color online) The relationships between relative error distributions of thumb bending angles and different numbers of synergies.

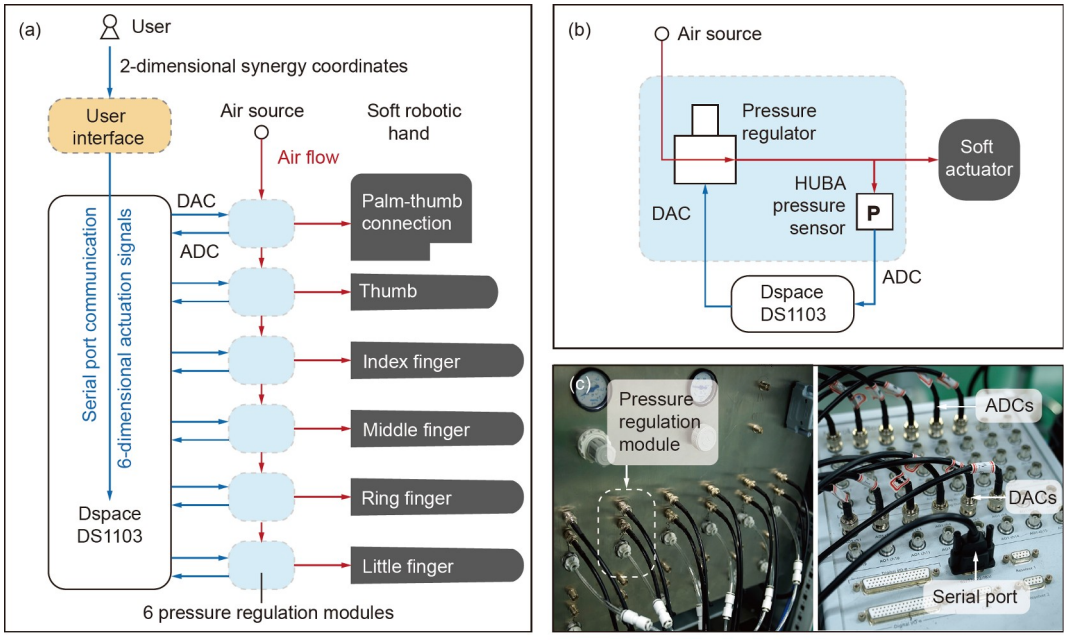

Figure 12 (Color online) A pneumatic control platform for the soft robotic hand. (a) Schematic of the control platform; (b) schematic of a single pressure regulation module; (c) pictures of the dSPACE-DS1103 control board and pneumatic components.

The pictures of the platform components are shown in Figure 12(c).

4.2 Motion characterization of the soft actuators

Based on the pneumatic control platform and the motion capture system, we investigate bending angle-pressure relationships for different soft actuators to obtain the numerical form of eq. (4) in Sect. 2.2. As shown in Figure 13(a), a total of three actuators are tested: index finger (as an example), thumb, and the thumb-palm connection. Index finger and thumb are mounted on a rigid base to avoid mutual interference between actuators. The thumb-palm connection is mounted on the soft robotic hand rather than mounted on a rigid base with free motion. That's because the thumb-palm connection locates between the palm skeleton and the skin, both constrain the free motion of the thumb-palm connection (see Figure 13(b)).

Actuator bending angles are recorded based on a visual tracking process. As shown in Figure 13(a), for the index finger, two reflective markers are attached to the base (termed base markers) and another two markers to the tip end (termed end markers). The base markers generate a reference position vector (termed RPV). The end markers generate a bending position vector (termed BPV, marked dot at 0 kPa and solid at the other pressures). The distributions of makers for the thumb and the thumb-palm connection are analogous to that of the index finger. At the initial state (i.e., 0 kPa), the actuator has an initial angle deviation (IAD) which is introduced by structural constraints, gravity, and fabrication deviations. IAD is denoted as θ_i (i=1,2,…,6) and is defined as the angle between RPV and BPV at 0 kPa. As shown in Figure 13(b), IADs of the index finger, thumb, and thumb-palm connection are measured 18°, 13°, and 35°, respectively.

Then, we pressurize the actuators from 0 to 80 kPa in 10 kPa increments and record BPVs at these pressures. The actuator bending angle $\hat{q}_i$ (i = 1, 2, ⋯, 6) at pressure σ (σ>0) kPa is denoted as the angle generated by the BPV at 0 kPa and the BPV at σ kPa. Note that $\hat{q}_2$ is the sum of the MCP joint and IP joint; $\hat{q}_i$ (i = 3, 4, 5, 6) is the sum of the MCP joint, PIP joint, and DIP joint. The still images of actuator bending at different pressures are shown in Figure 13(c). Generally, the actuator bending angle increases with

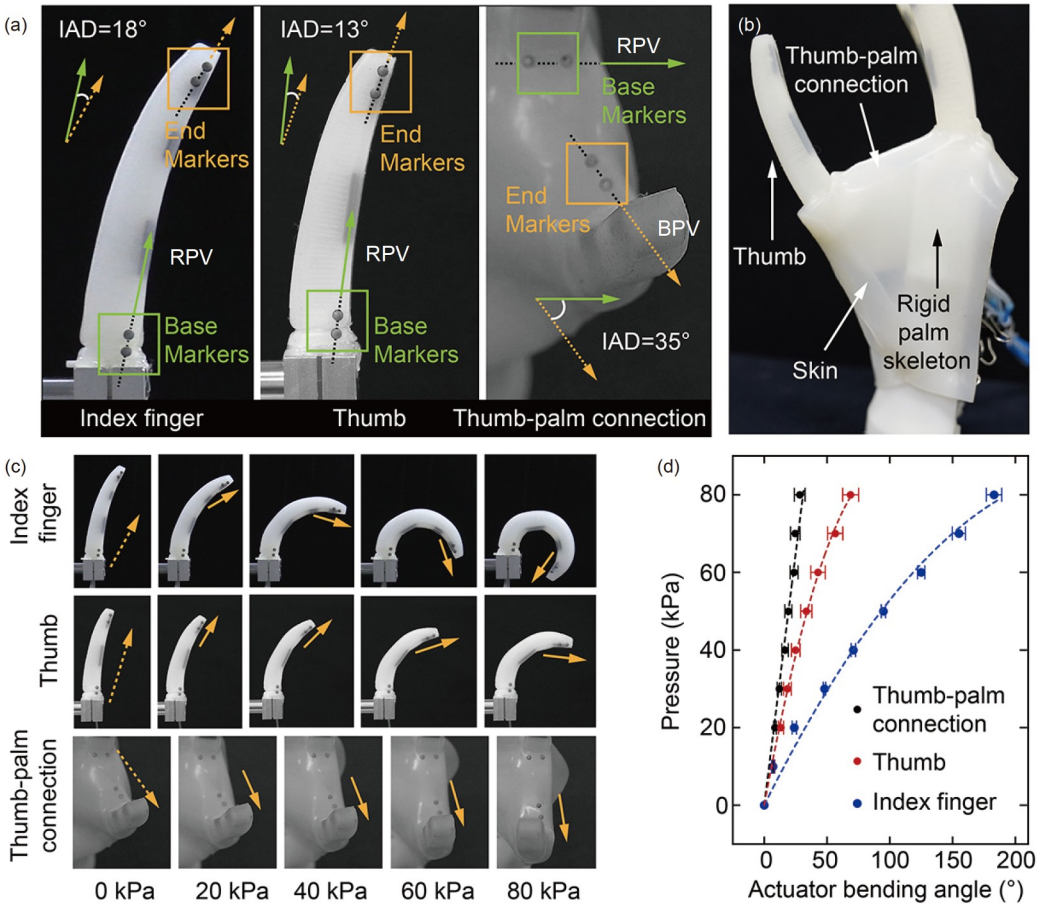

Figure 13 (Color online) Characterization of the soft actuators. (a) Illustration of IADs; (b) location of the thumb palm connection; (c) actuator motions upon pressurization; (d) bending angle-pressure relationships.

the pressure, and the actuator bending angle-pressure relationships are plotted in Figure 13(d). We further describe bending angle-pressure relationships for different actuators by polynomial fitting (the solid lines denote the fitting curves):

$$\begin{cases} \hat{p}_1 = 2.65146\,\hat{q}_1, \\ \hat{p}_2 = -0.00884\,\hat{q}_2 + 1.76401\,\hat{q}_2, \\ \hat{p}_i = -0.00128\,\hat{q}_i + 0.6583\,\hat{q}_i\ , \\ (i = 3,\ 4,\ 5,\ 6), \end{cases} \tag{21}$$

where $\hat{p}_i$ denotes pressure of the i-th actuator. The coefficients of determination (R-Squares) of the three models are 0.993, 0.999, and 0.997, which indicates that the models well explain the variations of measured values. The error bars are along the horizontal axis. To eliminate angle mismatches between the human fingers and the soft fingers, the actuator bending angle q_i in the task space can be calculated by

$$q_i = \hat{q}_i + \theta_i. \tag{22}$$

Therefore, we can calculate the required pressure p_i for the actuator bending angle q_i in the task space by combining eqs. (18) and (19):

$$\begin{cases} p_1 = 2.65146\,(q_1 - \theta_1), \\ p_2 = -0.00884\,(q_2 - \theta_2)^2 + 1.76401\,q_2, \\ p_i = -0.00128\,(q_i - \theta_i)^2 + 0.6583\,q_i\ , \\ (i = 3,\ 4,\ 5,\ 6). \end{cases} \tag{23}$$

4.3 Experimental methods and results

In this section, we perform experiments with the pneumatic control platform to demonstrate how the soft robotic hand replicates human-like grasp postures via the synergistic control approach. The soft robotic hand is fixed on a fixed base horizontally or vertically for the ease of executing grasp postures. For a certain grasp posture defined by the Feix taxonomy, we first enter its 2-dimensional synergy coordinates (x, y) (i.e., the plane coordinates in Figure 8) into the user interface. The interface calculates the required 6-dimensional pressure signals (p_1, p_2, p_3, p_4, p_5, p_6) by combining the synergy coordinates, eqs. (12)–(15), and (18)–(20). Then, these pneumatic actuation signals are sent to the dSPACE-DS1103 board to drive 6 actuators of the soft robotic hand to execute the corresponding grasp posture. In the above experimental process, all 6 actuators are driven simultaneously, which may cause thumb interference for some grasp postures.

To avoid thumb interference, we further program the time sequences of actuator pressures for different grasp postures (the required soft actuators' pressures are still (p_1, p_2, p_3, p_4, p_5, p_6)). For a certain grasp posture, an assistant passes an object (corresponding to the posture defined by the Feix taxonomy) to a proper position of the soft robotic hand. The proper position is in accordance with that of the human hand (as illustrated in Figure 5), and the assistant may adjust the proper position several times. The soft robotic hand then executes the corresponding posture with the programmed time sequences of actuator pressures to grasp the object (i.e., replication of the posture). We qualitatively evaluate the replication effectiveness of the posture by observing whether the object is steadily held over a period of time. We set the hold time as 10 s considering both the reliability and efficiency of the experiment. The posture replication is regarded as being failed if the object drops out in less than 10 s. On the contrary, the posture replication is regarded as being successful.

Here, we take the experiment of Tripod as an example, which involves four stages (see Figure 14(a)). In stage 0, the assistant starts to pass the ping pong ball to the proper position of the soft robotic hand, and no actuator is inflated. In

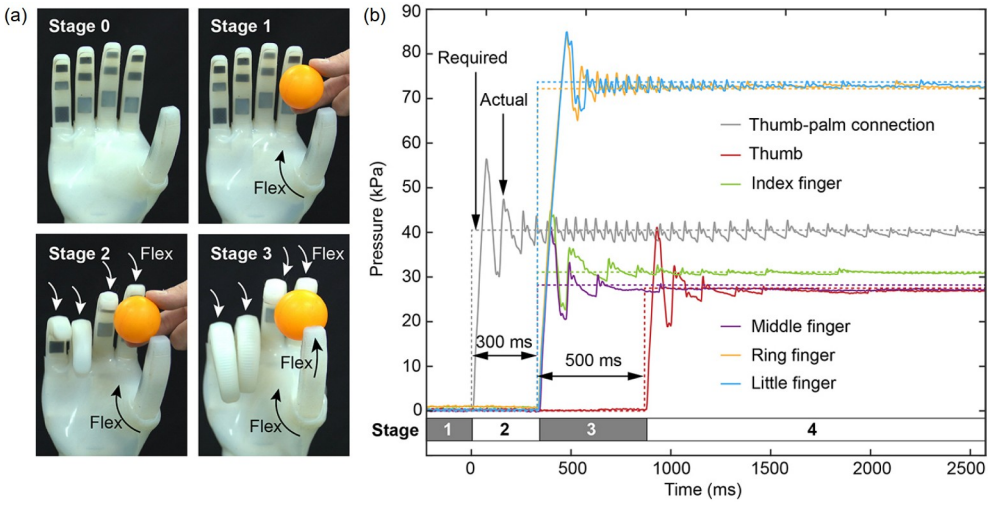

Figure 14 (Color online) The tripod experiment. (a) Still images of the four stages; (b) time-dependent pressure regulation of 6 actuators in the soft robotic hand.

stage 1, the thumb-palm connection starts to flex to offer circumduction for the thumb (p_1=41.2 kPa) . After 300 ms, stage 2 starts, where the index finger, middle finger, ring finger, and little finger flex towards the palm ((p_3, p_4, p_5, p_6)= (32.3, 27.8, 72.6, 73.7) kPa). After 500 ms, stage 3 starts, where the thumb flexes towards the palm (p_2=27.4 kPa). At this time, the ping pong ball is grasped by the soft robotic hand. The time sequences of actuator pressures are plotted in Figure 14(b). The required pressures and the actual pressures (measured by the HUBA sensor) are represented by dotted curves and solid curves, respectively. Although fluctuations exist in the actual pressure curves due to the abrupt switches of the bang-bang controller [35], the pneumatic flow rate (about 80 LPM) is large enough to compensate these fluctuations. As shown in Video S1, the soft robotic hand can execute reliable grasping without obvious vibrations. In the future, we will try to develop control strategies for more precise and smooth control.

We perform experiments of all 33 grasp postures (defined by the Feix taxonomy) on the soft robotic hand. As shown in Figure 15, 30 out of 33 grasp postures replication are successful (see Video S1 for representative grasp postures). The results demonstrate that the soft robotic hand can achieve most of the human-like grasp postures with merely the first 2 synergies, and the inherent compliance helps compensate for errors introduced by the absent synergies, the indirect DIP joint calculation, and the object position/orientation. For example, the relative errors of bending angles between $\widetilde{\mathbf{Q}}$ and $\mathbf{Q}$ are quite large for thumb-palm connection and thumb in Fixed Hook (see Figure 10). Such a large error is typically unacceptable for a rigid robotic hand driven by 2-dimensional synergy coordinates because the object is likely to be crushed by the rigid robotic hand. However, the error is acceptable for control of the soft robotic hand (at least in this case) because the excessive pressures in the thumb-palm connection and thumb do not harm the grasped object. In another example, Palmar pinch, the directions of thumb bending in $\mathbf{Q}$ and $\widetilde{\mathbf{Q}}$ are reverse (–10.5° vs. 29.4°), but the soft robotic hand can also successfully grasp the object with the inherent compliance of thumb. This interesting phenomenon is consistent with the results in ref. [13]. Figure 16 demonstrates the photo sequence of representative successful grasp postures, such as large diameter, distal type, tip pinch and palmar.

Failed grasp postures are writing tripod, tripod variation, and adduction grip. The reason for the failure of writing tripod and tripod variation is that they both require very sophisticated coordination motions between fingers. The reason for Adduction Grip is that no active adduction motion is provided by the index finger and middle finger. Alternatively, we can wedge the object between the fingers ((p_3, p_4)=(0,0) kPa) and inflate the fingers ((p_3, p_4)=(60,60) kPa) to bend. The sidewalls of bending fingers have higher stiffnesses (compared with those of the fingers at 0 kPa) to prevent the object from dropping out. In this sense, the posture can be considered been invoked by the hand architecture and achieved by the actions of the finger themselves.

5 Conclusions

This paper presents a synergistic control approach for soft robotic hands to achieve coordinated, human-like grasp postures based on recorded human finger joint angles. First, we develop a kinematic model of the robotic hand (with 6 soft, inflatable actuators) to describe its output postures and input parameters. As the input parameters form a high-dimensional space, we leverage a PCA method to reproduce it with a low-dimensional space formed by synergies. To determine the human hand-robotic hand mapping, we conduct a human subject study in which the subject is requested to perform 33 grasp postures in the Feix taxonomy and his hand

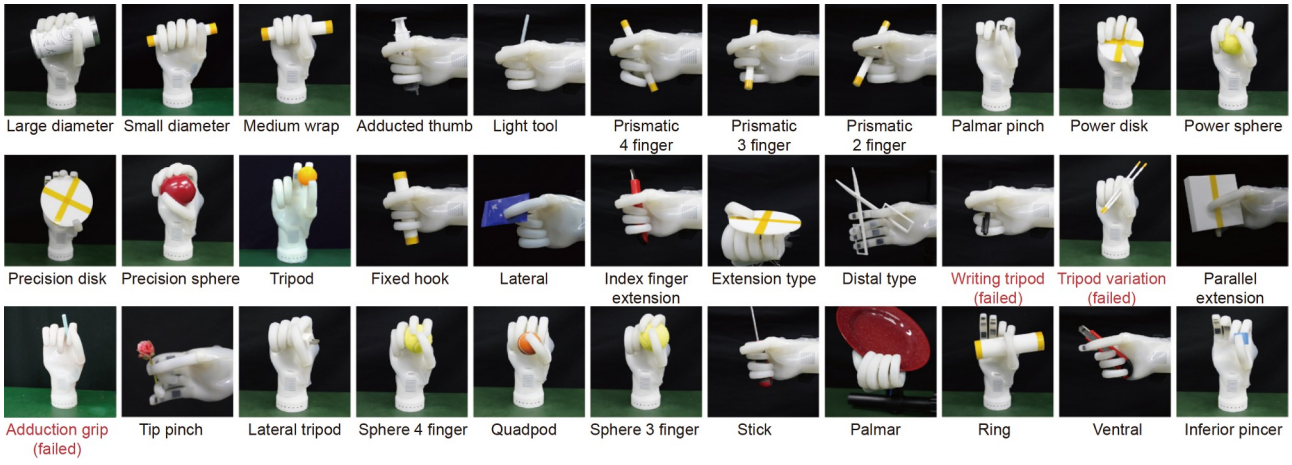

Figure 15 (Color online) Still images of the 33 grasp postures of the soft robotic hand.

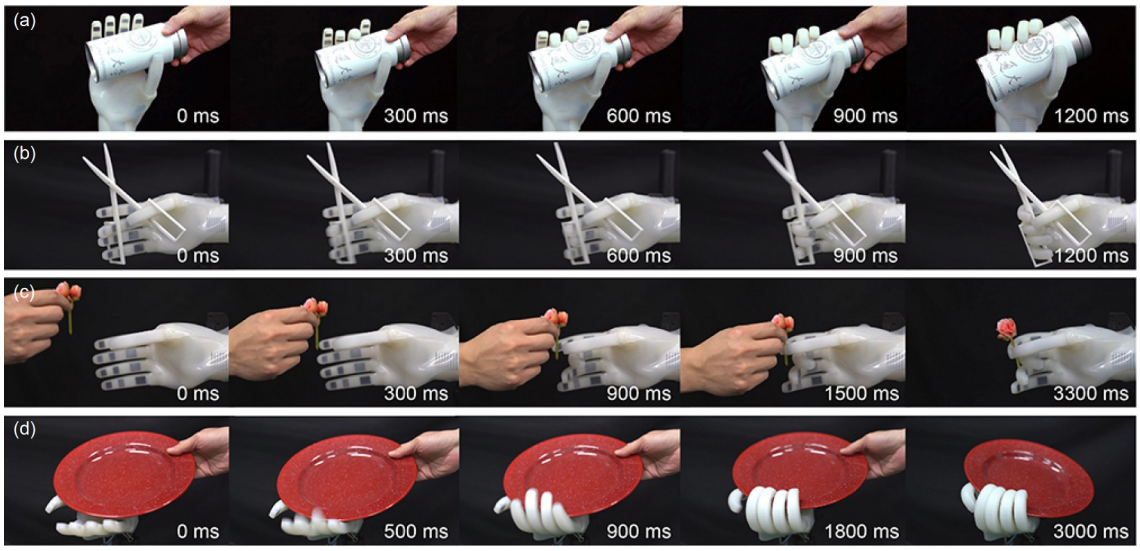

Figure 16 (Color online) Photo sequence of representative grasp postures. (a) Large diameter; (b) distal type; (c) tip pinch; (d) palmar.

joint angles are recorded to generate a dataset. PCA of the dataset reveals that the first 2 synergies count for 89.9% cumulative contribution of angle variance, which indicates that 2-dimensional synergy coordinates can be used as inputs to control the soft robotic hand. An experimental platform is built to validate the effectiveness of the synergistic control approach, along with the nonlinear motion characterization of the soft actuators. The experimental results demonstrate that the soft robotic hand is able to reliably replicate 30 human-like grasp postures with the 2-dimensional control inputs and the help of inherent compliance.

The limitation of our approach is that the complexity of mechanical hardware (e.g., actuators and valves) is not reduced. Future work will focus on exploiting the mechanical implementation of postural synergies, which is expected to take full advantage from the capabilities of soft robotic hands. We will also investigate the possibility of using the proposed approach for other human-involved applications such as prostheses, manipulation, and human-machine interactions.

This work was supported by the National Natural Science Foundation of China (Grant Nos. 52025057, 91948302), and the Science and Technology Commission of Shanghai Municipality (Grant No. 20550712100).

Supporting Information

The supporting information is available online at tech.scichina.com and link.springer.com. The supporting materials are published as submitted, without typesetting or editing. The responsibility for scientific accuracy and content remains entirely with the authors.

1 Piazza C, Grioli G, Catalano M, et al. A century of robotic hands. Ann Rev Control Robot Autonom Syst, 2019, 2: 1–32
2 Jacobsen S C, Wood J E, Knutti D F, et al. The UTAH/M.I.T. Dextrous hand: Work in progress. Int J Robotics Res, 1984, 3: 21–50
3 Butterfaß J, Grebenstein M, Liu H, et al. DLR-hand II: Next generation of a dextrous robot hand. In: Proceedings of the 2001 IEEE International Conference on Robotics and Automation (ICRA). Seoul, 2001. 109–114
4 Palli G, Melchiorri C, Vassura G, et al. The DEXMART hand: Mechatronic design and experimental evaluation of synergy-based control for human-like grasping. Int J Robotics Res, 2014, 33: 799–824
5 Shadow Robot Company. Dexterous hand series: The world's most dexterous humanoid robot hands. 2021, https://www.shadowrobot.com/products/dexterous-hand
6 Baril M, Laliberté T, Gosselin C, et al. On the design of a mechanically programmable underactuated anthropomorphic prosthetic gripper. J Mech Des, 2013, 135: 209–219
7 Dollar A M, Howe R D. The highly adaptive SDM hand: Design and performance evaluation. Int J Robotics Res, 2010, 29: 585–597
8 Deimel R, Brock O. A novel type of compliant and underactuated robotic hand for dexterous grasping. Int J Robotics Res, 2016, 35: 161–185
9 Zhao H, O'Brien K, Li S, et al. Optoelectronically innervated soft prosthetic hand via stretchable optical waveguides. Sci Robot, 2016, 1: eaai7529
10 Zhou J, Chen X, Chang U, et al. A Soft-robotic approach to anthropomorphic robotic hand dexterity. IEEE Access, 2019, 7: 101483–101495
11 Teeple C B, Koutros T N, Graule M A, et al. Multi-segment soft robotic fingers enable robust precision grasping. Int J Robotics Res, 2020, 39: 1647–1667
12 Zhang N, Ge L, Xu H, et al. 3D printed, modularized rigid-flexible integrated soft finger actuators for anthropomorphic hands. Sens Actuat A-Phys, 2020, 312: 112090
13 Zhang Y, Zhang N, Hingorani H, et al. Fast-response, stiffness-tunable soft actuator by hybrid multimaterial 3D printing. Adv Funct Mater, 2019, 29: 1806698
14 Shao Q W, Zhang N B, Shen Z Q, et al. A pneumatic soft gripper with configurable workspace and self-sensing. In: Proceedings of the 2020 17th International Conference on Ubiquitous Robots (UR). IEEE, 2020. 36–43
15 Niiyama R, Sun X, Sung C, et al. Pouch motors: Printable soft actuators integrated with computational design. Soft Robotics, 2015, 2: 59–70
16 Galloway K C, Becker K P, Phillips B, et al. Soft robotic grippers for biological sampling on deep reefs. Soft Robotics, 2016, 3: 23–33
17 Brown E, Rodenberg N, Amend J, et al. Universal robotic gripper

based on the jamming of granular material. Proc Natl Acad Sci USA, 2010, 107: 18809–18814
18 Tsoli A, Jenkins O C. 2D subspaces for user-driven robot grasping. In: Proceedings of the Robotics, Science and Systems Conference: Workshop on Robot Manipulation. Atlanta, 2007, 2: 7–2
19 Santello M, Flanders M, Soechting J F. Postural hand synergies for tool use. J Neurosci, 1998, 18: 10105–10115
20 Wimböck T, Jahn B, Hirzinger G. Synergy level impedance control for multifingered hands. In: Proceedings of the 2011 IEEE/RSJ International Conference on Intelligent Robots and Systems (IROS). IEEE, 2011. 973–979
21 Matrone G C, Cipriani C, Secco E L, et al. Principal components analysis based control of a multi-dof underactuated prosthetic hand. J NeuroEng Rehabil, 2010, 7: 1–3
22 Kent B A, Karnati N, Engeberg E D. Electromyogram synergy control of a dexterous artificial hand to unscrew and screw objects. J Neuroeng Rehabil, 2014, 11: 1–21
23 Brown C Y, Asada H H. Inter-finger coordination and postural synergies in robot hands via mechanical implementation of principal components analysis. In: Proceedings of the IEEE/RSJ International Conference on Intelligent Robots and Systems (IROS). Cagliari, 2007. 2877–2882
24 Xu K, Liu H, Du Y, et al. Design of an underactuated anthropomorphic hand with mechanically implemented postural synergies. Adv Robotics, 2014, 28: 1459–1474
25 Xiong C H, Chen W R, Sun B Y, et al. Design and implementation of an anthropomorphic hand for replicating human grasping functions. IEEE Trans Robot, 2016, 32: 652–671
26 Catalano M G, Grioli G, Farnioli E, et al. Adaptive synergies for the design and control of the Pisa/IIT SoftHand. Int J Robotics Res, 2014, 33: 768–782
27 Gu G, Zhang N, Xu H, et al. A soft neuroprosthetic hand providing simultaneous myoelectric control and tactile feedback. Nat Biomed Eng, 2021, doi: 10.1038/s41551-021-00767-0
28 Feix T, Romero J, Schmiedmayer H B, et al. The GRASP taxonomy of human grasp types. IEEE Trans Hum-Mach Syst, 2016, 46: 66–77
29 Bohg J, Morales A, Asfour T, et al. Data-driven grasp synthesis—A survey. IEEE Trans Robot, 2013, 30: 289–309
30 Wold S, Esbensen K, Geladi P. Principal component analysis. Chemometrics Intelligent Laboratory Syst, 1987, 2: 37–52
31 Stewart G W. On the early history of the singular value decomposition. SIAM Rev, 1993, 35: 551–566
32 Kamper D G, Cruz E G, Siegel M P. Stereotypical fingertip trajectories during grasp. J NeuroPhysiol, 2003, 90: 3702–3710
33 Fujiki R, Arita D, Taniguchi R I. Real-time 3D hand shape estimation based on inverse kinematics and physical constraints. In: Proceedings of the International Conference on Image Analysis and Processing. Cagliari, 2005. 850–858
34 Magenes G, Passaglia F, Secco E L. A new approach of multi-dof prosthetic control. In: Proceedings of the 2008 30th Annual International Conference of the IEEE Engineering in Medicine and Biology Society. Vancouver, 2008. 3443–3446
35 Bellman R, Glicksberg I, Gross O. On the “bang-bang” control problem. Quart Appl Math, 1956, 14: 11–18